Low-velocity impact behaviour and failure of stiffened steel plates

G. Gruben[1,2,3*], S. Sølvernes[1,4], T. Berstad[1,2], D. Morin[1,2], O.S. Hopperstad[1,2] and M. Langseth[1,2]

[1]Centre for Advanced Structural Analysis, Centre for Research-based Innovation (CRI), NTNU, Norwegian University of Science and Technology, NO-7491 Trondheim, Norway

[2]Department of Structural Engineering, NTNU, Norwegian University of Science and Technology, NO-7491 Trondheim, Norway

[3]SINTEF Materials and Chemistry, Rich. Birkelands vei 2B, NO-7491 Trondheim, Norway

[4]GE Oil & Gas, Sluppenvegen 12B, NO-7037 Trondheim, Norway

Abstract

The behaviour and failure of stiffened steel plates subjected to transverse loading by an indenter is studied in this paper. Low-velocity dynamic and quasi-static tests of stiffened plates with geometry adopted from a typical external deck area on an offshore platform were conducted. The results show that the quasi-static tests provide a good reference for impact loading situations, although they displayed a larger displacement at fracture. Finite element simulations of the steel panel tests were performed, using the elastic-viscoplastic J_2 flow theory and a one-parameter fracture criterion. A relatively fine spatial discretization in the load application area was needed to capture accurately the onset of fracture. In order to locally refine the mesh, a method for automatic mesh refinement based on damage driven h-adaptivity was implemented and evaluated against results obtained with fixed meshes of various element sizes.

Keywords: Impact load; Stiffened plates; Finite element method; Fracture

1 Introduction

Stiffened plates are widely used structural parts in for instance platform and ship decks as well as in ship hulls [1], and constitute an important structural component when considering accidental loads such as low-velocity impact. Low-velocity impact loading, which can be defined as loading situations where the impact velocity is less than 25 m/s [2], may stem from

* Corresponding author. Tel.: + 47 48282291

E-mail address: gaute.gruben@sintef.no (G. Gruben).

for example dropped objects, ship grounding or ship-ship collisions [3]. In structural design for impact loads, hand calculations may lead to large costs as conservative assumptions likely have to be made. On the other hand, structural design by use of non-linear finite element analysis has the potential of achieving more cost efficient and safe structures. However, impact problems involve large deformations, plasticity, strain localization and fracture, phenomena which are not easy to model and simulate numerically with high accuracy and robustness [1]. In order to establish guidelines for design of structures subjected to impact loading by use of non-linear finite element analysis, a profound understanding of the physical phenomena and the numerical tools is needed. This can be achieved by conducting well instrumented experiments and based on these validating numerical simulation models [4]. Experimental data from full-scale impact tests are rare and expensive and such tests are restricted when it comes to instrumentation. Benchmark tests, on the other hand, can be conducted relatively inexpensively under controlled conditions and with appropriate instrumentation in a laboratory. The benchmark test has to incorporate the relevant physical phenomena which are to be captured in a full-scale structure, and has to be supported by material tests to ensure correct material input in the numerical simulation model.

Extensive research has been conducted over the last decades on unstiffened plates subjected to low-velocity impact loading, e.g. [5-10]. The effects of the boundary conditions, the shape of the indenter, the plate material and the velocity and mass of the indenter have been investigated. In some studies, low-velocity impact tests have been compared with tests conducted under quasi-static loading. Langseth and Larsen [11] carried out an experimental study on the plugging capacity of fixed and simply supported square-shaped St-52 steel plates under low-velocity and quasi-static loading by a circular blunt-edged punch. It was found that the critical contact force between plate and punch was approximately the same for low-velocity and quasi-static loads, and that the material's strain rate sensitivity could be neglected in the structural design. Gruben et al. [12] conducted low-velocity and quasi-static punch tests on dual-phase and martensitic steel sheets. The experiments shared similarities with the Nakajima formability tests [13], and covered stress states ranging from uniaxial tension to equi-biaxial tension. It was found that the response in terms of force-displacement curves and strain histories at critical locations were similar for low-velocity and quasi-static loading, independent of material and specimen geometry.

Langseth and Larsen [14] investigated the plugging capacity of stiffened steel panels subjected to a dropped drill collar which hit the panels between the stringers. The results of these experiments were compared with results from tests carried out under quasi-static loading and from tests on unstiffened plates. It was found that stiffening a plate with stringers did not influence the critical impact energy compared to a single plate, and that the static and dynamic force-displacement curves of the stiffened plates were approximately equal. Alsos and Amdal [15] conducted experiments on one unstiffened steel plate and four types of stiffened steel plates subjected to quasi-static transverse loading by a cone-shaped indenter. It was found that for increasing stiffness, the indentation at initial fracture decreased. However, the stiffened plates displayed significant post-fracture resistance. Liu et al. [16] presented experiments where stiffened steel plates were quasi-statically loaded at the mid-span by two different type of indenters. Numerical models of the experiments were validated, and gave information on the energy absorption of the different structural components. Cho and Lee [17] carried out impact tests on 33 stiffened steel plates. The impact velocity and mass were in the range 1.6-6.1 m/s and 42-574 kg, respectively, and the plate thickness and the number and design of the stiffeners were varied. The results were applied to validate a simplified analytical model for predicting the extent of damage in the stiffened plates.

Several studies show that the J_2 flow theory, based on the von Mises yield function, the associated flow rule and isotropic hardening, gives an adequate description of steel materials [18-21], although strain-rate and temperature effects have to be accounted for in some cases. When it comes to the prediction of ductile fracture in metallic materials, several models exist in literature. In some models the material damage is influencing the constitutive equations, e.g. [22-24], while in other models, the yield criterion, plastic flow and strain hardening are unaffected by the damage, e.g. [25-29]. In impact simulations of large structures such as ship collisions, the most applied ductile fracture criterion is the critical value of the equivalent plastic strain [30], sometimes referred to as the fracture strain. This criterion does not account for the stress-state dependence of the material's ductility, but has been applied successfully in several studies, e.g. [31-33]. Failure can also be predicted by forming limit diagrams which can be strain based [34] or stress based, e.g. [35, 36]. Alsos et al. [37] applied a stress-based forming limit criterion (denoted the BWH criterion) to predict incipient necking in stiffened steel plates. The results were generally in good agreement with the experimental results [15].

Since stiffened plates usually are parts of a large structure such as an offshore platform or a ship, the size of the structure puts restrictions on the spatial discretization in full-scale finite element simulations due to computational costs. This leads to challenges in the fracture modelling as the numerical fracture strain is strongly dependent on the element size. To cope with this, various modifications of Barba's law have been applied for scaling the fracture strain as function of the element size, e.g. [38-40]. Ehlers et al. [39] performed finite element simulations of the collision response of three different ship-side structures and found that the mesh-size sensitivity might be more important than the fracture criterion itself for the cases investigated. To deal with the element size problem, a method for calibrating the true stress-strain curves as well as the fracture strain based on the element length was proposed [41]. Storheim et al. [42] presented a failure model where a mesh-size dependent, post-necking damage evolution rule is coupled with the constitutive model after predicting onset of necking according to the BWH criterion. The failure model was validated against experiments at different scales and proved to exhibit good accuracy and robustness.

In this study, the structural response of stiffened steel panels under low-velocity impact loading is investigated and compared with similar quasi-static test. The experimental results are used to assess a finite element model of the stiffened panels in which the steel material is modelled with the elastic-viscoplastic J_2 flow theory and a one-parameter fracture criterion. A method for mesh refinement based on h-adaptively is proposed for handling fracture in large-element simulations.

2 Material tests

The specimens applied in this study are cut from 3 mm plates of Domex 355 MC E, which is a hot-rolled, low-alloy steel with minimum yield strength of 355 MPa. The material consists of a ferritic (bcc) crystalline structure, and displays good welding, cold forming and cutting performance. Thus, the material is well suited for offshore structures. The chemical composition of the material is given in Table 1.

Three tensile specimens, cut in the rolling direction of the steel plate, were tested under displacement control in an Instron 5982 tensile testing machine. The nominal geometry of the test specimen is given in Fig. 1(a). The crosshead velocity was 5 mm/min, giving a nominal strain rate of $1.2 \cdot 10^{-3}$ s^{-1}. The initial width and thickness along the gauge length of each specimen were measured at three different locations by a Vernier calliper, and no significant variation was observed. From optical measurements, a virtual extensometer was applied to measure the displacement. Images were taken by a Nikon camera with a 105 mm Sigma lens at a framing rate of 1 Hz. Before testing, the specimen was spray-painted with a speckle pattern to enhance point tracking, and the displacement field was generated by postprocessing the images by an in-house Digital Image Correlation software [43]. The force history was recorded by the load cell of the tensile testing machine at a framing rate synchronized with the camera recordings. The engineering stress was calculated as $s = F / A_0$, where F is the measured force and A_0 is the measured initial cross-section area. The engineering strain was calculated as $e = L / L_0 - 1$, where L is the extensometer length and $L_0 = 30$ mm is the initial extensometer length. The true stress, σ, true strain, ε, and true plastic strain, ε^p, before onset of diffuse necking were calculated as $\sigma = s\left(1+e\right)$, $\varepsilon = \ln\left(1+e\right)$ and $\varepsilon^p = \varepsilon - \sigma / E_m$, where E_m is the measured Young's modulus from the true stress-strain curve in each test. In the three tests, E_m was found to be 175 ± 1 GPa. Note, however, that a more accurate test method is needed to identify Young's modulus, which is likely closer to 210 GPa for steel. The engineering stress-strain curves are shown in Fig. 1(b), while Fig. 1(c) shows the true stress-plastic strain curves up to necking.

The width and thickness was measured post-mortem in the tensile specimens at a location 35 mm from the centre necking zone in the longitudinal direction. From these measurements, the Lankford coefficient was estimated as $R = \varepsilon_W^p / \varepsilon_T^p$, where ε_W^p and ε_T^p are in turn the true plastic strain at diffuse necking in the width and thickness directions of the specimen. All three tests gave $R = 0.85$, which indicates a slight plastic anisotropy. Tensile tests were not conducted in other directions of the sheet, and in the material modelling we will assume the material to be quasi-isotropic.

3 Component tests

The design of the stiffened steel plate components represents a scaled version of a typical external deck on an offshore platform. Such platform deck may consist of a ~12 mm thick stiffened steel plate supported by girders positioned 3-4 m apart in the length direction and ~10 m apart in the width direction. Further, the plate may be stiffened with bulb flats oriented in the direction of the shortest span with centre distances of ~0.5 m. Due to limitations of the laboratory equipment, it was decided to perform the tests in scale 1:4. Two different indenters were applied to study the effect of a relatively large-sized object striking the plate field and a more locally applied load between the stringers. Tests were carried out under low-velocity dynamic and quasi-static loading. The loading rate in the low-velocity dynamic tests was approximately 30000 times larger than in the quasi-static tests. Each test was assigned a unique label XX-YZ, where XX stands for low velocity (LV) or quasi-static (QS) loading, Y denotes the indenter type (C = cylindrical, or H = hemispherical) and Z gives the duplicate number. Table 2 gives an overview of the conducted tests.

3.1 Specimen geometry and boundary conditions

The test specimen is a 3 mm thick rectangular plate with dimensions $1250\ \text{mm} \times 1375\ \text{mm}$, stiffened by six stringers in the transverse direction, as shown in Fig. 2(a) and (b). The stringers have an L-shaped cross-section with a height of 65 mm, a width of 18 mm and a nominal thickness of 3 mm. Details of the stringer cross-section are given in Fig. 2(c). The stringers were fastened to the plate by intermittent fillet welds with a throat size of 3 mm, a weld length of 15 mm, and a centre-to-centre distance of 45 mm, see Fig. 2(d).

Before testing, the specimen was placed into a test rig frame consisting of two support frames constructed from SHS100x10 members. Details of the test rig frame are presented in Fig. 3. The support frames were clamped by 8 M16 bolts in property class 12.9. The bottom frame had 50 mm wide and 70 mm deep cut-outs so that the stringers could be continuous along the width of the plate, see Fig. 3(d). Additionally, 8 mm thick L-shaped shim plates were placed between the bottom frame and the specimen. This way the gap around the stringer was reduced from 50 mm to approximately 10 mm, see Fig. 3(d). Due to the cut-outs, additional SHS100x10 members were welded to the longitudinal beams in the bottom frame to increase the stiffness, see Fig. 3(e). Teflon sheets with 3 mm thickness were added at the specimen-top frame and specimen-shim plate interfaces, as illustrated in Fig. 3(d).

In each test, the specimen was loaded transversely at the geometrical centre. Two types of indenter geometries were used in this study. The first indenter, denoted indenter C, is cylindrical with hemispherical caps at its two ends, see Fig. 4(a). The length of 350 mm is sufficient to ensure that contact occurs directly above two of the centre stringers of the plate field which results in deformation over a relatively large part of the steel panel. The second indenter, denoted indenter H, is hemispherical, as shown in Fig. 4(b), and used to study the effect of a more locally applied load between the stringers.

3.2 Quasi-static tests

Two duplicate quasi-static tests were conducted for each of the two indenters in the rig illustrated in Fig. 5(a). Plate indentation was enforced by a 1000 kN capacity hydraulic jack from R.D.P. Howden Ltd. run under displacement control at a rate of 10 mm/min. An HPM U15/1MN load cell was attached to the cross head of the cylinder to measure the contact force towards the plate. Due to the large forces and the size of the test rig, the displacement measurements taken from the position of the load cell may be influenced by machine stiffness. To circumvent this, the relative displacement between the load cell and the bottom support frame was measured. Two optical displacement sensors with a measuring range of 200 mm were attached to the mid span of the bottom frame beams; the position of one of the sensors is illustrated in Fig. 5(b). The target for the optical displacement sensors was a horizontal bar attached to the load cell, as shown in Fig. 5(a) and (b).

3.3 Low-velocity impact tests

The low-velocity impact tests of the stiffened steel panels were conducted in a pendulum impactor depicted in Fig. 6(a) [44]. The four legs of the lower support frame were fastened to the reaction wall by welds, as shown in Fig. 6(b) and (c). The impacting mass consisted of a trolley equipped with a load cell and the indenter, as illustrated in Fig. 6(d). One test was conducted with the cylindrical indenter, while three duplicates were carried out with the hemispherical indenter. The load cell recorded the force $P(t)$ at 200000 Hz, while the impact velocity of the trolley, v_0, was measured by a system of photocells located directly in front of the specimen, see Fig. 6(a) and (b). Two high-speed cameras, Fig. 6(e), recorded the tests at 15000 Hz, thus providing about 450-750 data points in each test. One camera was positioned perpendicularly to the loading direction, and the digital images from this camera were used to determine the velocity and displacement of the trolley during the impact. To this end, a patch with a chessboard pattern was fastened to the load cell, see Fig. 6(f), and the positions of two points were tracked using the Harris and Stephens corner detection algorithm [45]. The pixel/mm ratio was established from the known distance between the two tracking points. As rubber pads are positioned between the floor and the reaction wall, movement of the reaction wall may occur during testing. During the tests, a laser tracked the relative position of the reaction wall with respect to the floor, and no displacement of the reaction wall was found.

The displacement was also calculated from data obtained from the force signal in the load cell. Under the assumption that the trolley, load cell and indenter translated as a rigid body, the acceleration, $\ddot{u}(t)$, velocity, $\dot{u}(t)$, and displacement, $u(t)$, of the impacting mass were found from the force measurement in the load cell, $P(t)$, and the initial velocity of the trolley as

$$\ddot{u}(t) = -\frac{P(t)}{M_T}, \quad \dot{u}(t) = v_0 + \int_0^t \ddot{u}(t)\,dt, \quad u(t) = \int_0^t \dot{u}(t)\,dt \tag{1}$$

Here, $M_T = 1383\ \text{kg}$ is the mass of the trolley and the part of the load cell behind the strain gauge used in the force measurement, see [12] for details. The displacement recording from the load cell was in agreement with the displacement recording from the high-speed camera. The force between the specimen and the indenter was estimated as

$$F(t) = \left(1 + \frac{M_P}{M_T}\right) P(t) \tag{2}$$

where M_P is the mass of the indenter and the part of the load cell in front of the strain gauge. The mass M_P was equal to 69.3 kg and 46.2 kg for the cylindrical and hemispherical indenter, respectively. According to Eq. (2), the force between the indenter and the specimen is in turn 5.0% and 3.3% larger than the measured force in the load cell for the cylindrical and hemispherical indenter.

3.4 Experimental results

Fig. 7(a) shows the final deformation of the quasi-static test QS-C1 with the cylindrical indenter, where buckling occurred at the plate boundaries between the central stringers. This type of buckling was observed in all the component tests, independent of indenter shape and loading rate. The buckles had a sinusoidal shape, as illustrated in Fig. 7(b), with amplitude spanning from 3 mm to 5 mm in the different tests.

In the tests conducted with the cylindrical indenter, the two central stringers experienced inward lateral torsional displacement, as indicated in the case of the QS-C1 test in Fig. 7(a). This test was stopped before fracture occurred. The other quasi-static test QS-C2 was loaded to a lower maximum force level, while the maximum force level in the low-velocity test LV-C1 was between the maximum force in the QS-C1 and QS-C2 tests. Fig. 8(a) shows the force-displacement curves from the tests with the cylindrical indenter. The final deformation mode in all tests with this indenter was similar to the deformation mode shown in Fig. 7(a) for the QS-C1 test. However, the QS-C2 and LV-C1 tests had smaller deformations as they were subjected to less external loading.

All the tests conducted with the hemispherical indenter penetrated the specimen, with an exception of the low-velocity test LV-H3 with $v_0 = 4.49\ \text{m/s}$ in which the impactor had slightly less kinetic energy than what was needed to initiate failure. Fig. 8(b) shows the force-displacement curves from the tests with the hemispherical indenter. Notably the quasi-static tests displayed a larger displacement at fracture than the low-velocity tests. In the quasi-static tests, local necking occurred ~23 mm in the radial direction from the apex of the indenter, see Fig. 7(c), followed by crack propagation ending in a fracture pattern as the one presented in Fig. 7(d). Fig. 7(c) and (d) are taken from the quasi-static test QS-H1 and the time between the images is 1.0 s, which corresponds to an indenter displacement of 0.17 mm. The development of the fracture between these two images was not captured. However, based on previous experience [12], it is believed that fracture initiated in the neck before a primary crack propagated as a slant shear fracture from the neck in the directions shown by the white arrows in Fig. 7(d) and indicated in Fig. 7(e). Further, it is assumed that a secondary crack was formed in the necking region and propagated as a slant shear fracture in the radial direction, as indicated by the red arrow in Fig. 7(d) and shown in Fig. 7(f). The fracture mode in the low-velocity tests differed somewhat from the fracture mode in the quasi-static tests. The low-velocity tests also exhibited local necking prior to fracture as demonstrated for the LV-H1 specimen in Fig. 7(g), but here two secondary cracks formed in the radial direction, as indicated by the red arrows. The fracture mode in the low-velocity tests have some similarities with the petalling mode observed in several plate impact studies, e.g. [46-48]. In all tests with the hemispherical indenter, the two centre stringers were pushed outward in the centre of the plate during the indentation, as can be observed for the LV-H1 test in Fig. 7(g).

As can be seen from Fig. 8(a) and (b), the low-velocity tests display a higher force level than the quasi-static tests, an effect that may stem from the material's strain-rate sensitivity since the striking mass is significantly larger than the mass of the target. The difference in force level between the low-velocity and quasi-static tests is larger in the tests with the cylindrical indenter than in those with the hemispherical indenter. This may be due to the smaller region of the specimen subjected to plastic deformation in the tests with the hemispherical indenter. Fig. 8(c) and (d) compares the force-displacement response obtained with the two indenters. The tests with the hemispherical indenter exhibit lower stiffness, which again indicates that a smaller part of the specimen is activated in the resistance of the applied load. Notably all the tests with the cylindrical indenter produce a springback after peak force, see Fig. 8(a), since the panels were not penetrated. The same applies for the low-velocity test with the hemispherical indenter and $v_0 = 4.49$ m/s (LV-H3). The time durations of the low-velocity tests were ~30 ms in the two tests were the indenter penetrated the specimen and ~50 ms in the two tests where the indenter rebounded from the specimen.

4 Numerical analysis

4.1 Material model

The elastic properties of the steel panels were described by a Young's modulus of 210 GPa and a Poisson ratio of 0.3, and the material density was set to 7850 kg/m^3. The inelastic behaviour of the material was modelled by the rate-dependent (or viscoplastic) J_2 flow theory. The dynamic yield function is given in the form

$$f = \sigma_{VM}(\mathbf{s}) - \sigma_f(p, \dot{p}) = 0 \tag{3}$$

where $\sigma_{VM} = \sqrt{\frac{3}{2}\mathbf{s}:\mathbf{s}}$ is the von Mises equivalent stress and $\mathbf{s}$ is the deviatoric part of the Cauchy stress tensor. The flow stress σ_f is defined by

$$\sigma_f = \begin{cases} \sigma_0\left(1+\dfrac{\dot{p}}{\dot{p}_0}\right)^c & \text{for} \quad p \le p_L \\ K\left(p+p_0\right)^n\left(1+\dfrac{\dot{p}}{\dot{p}_0}\right)^c & \text{for} \quad p > p_L \end{cases} \tag{4}$$

where $\dot{p}$ is the equivalent plastic strain-rate which is work conjugate with σ_{VM}, $p = \int \dot{p}\,dt$ is the equivalent plastic strain, σ_0 is the yield stress, and K and n are parameters governing the work hardening. The equivalent plastic strain at the end of the Lüders plateau is given by p_L, while the parameter $p_0 = (\sigma_0 / K)^{1/n} - p_L$ enforces continuity of the stress-strain curve at $p = p_L$. The parameters c and $\dot{p}_0$ define the strain-rate sensitivity of the material. By neglecting the viscoplastic strengthening factor in Eq. (4), the Considère criterion predicts diffuse necking in uniaxial tension at $p = n - p_0$.

The work hardening parameters in Eq. (4) were fitted to the true stress-plastic strain curves from the uniaxial tensile tests up to incipient necking, as shown in Fig. 1(c). Material testing at elevated strain rates was not conducted in this study. Instead, the values of the parameters c and $\dot{p}_0$ identified for a martensitic steel in [12] were found appropriate and used in the simulations. The constitutive parameters are summed up in Table 3.

The calibrated material model was applied in simulations of the uniaxial tensile tests run with the implicit solver of LS-DYNA [49]. The specimen was discretized by fully-integrated solid elements (LS-DYNA Type −2). A converged solution for the engineering stress-strain curve was achieved with a characteristic element size of 0.2 mm in the gauge region. A prescribed velocity was applied to the rigid parts sharing nodes with the deformable region, see Fig. 9(a). The prescribed velocity was ramped up to 2.5 mm/min over the first 12 s of the simulation using a smooth transition function. Thus, the gauge region experienced a pre-necking strain rate of $1.2 \cdot 10^{-3}$ s^{-1} like in the experiments. The total simulation time was 300 s. As can be seen from Fig. 1(b), a reasonable correlation between the experimental and numerical engineering stress-strain curves was obtained. A better agreement in the post-necking region of the engineering stress-strain curves could potentially have been obtained by use of inverse modelling, but this was not deemed necessary for the current application. Notably a simulation without rate-dependence resulted in an overly rapid decrease of the post-necking stress level, as shown in Fig. 1(b).

Ductile fracture was modelled by the Cockcroft-Latham (CL) criterion [25]

$$W = \int_0^p \langle \sigma_I \rangle \, dp \le W_C, \quad \langle \sigma_I \rangle = \max\left(\sigma_I, 0\right) \tag{5}$$

where W_C is the fracture parameter. The major principal stress σ_I is given by [28]

$$\sigma_I = \left(\sigma^* + \frac{3-\mu}{3\sqrt{3+\mu^2}} \right) \sigma_{VM} \tag{6}$$

where $\sigma^* = \frac{1}{3}(\sigma_I + \sigma_{II} + \sigma_{III}) / \sigma_{VM}$ is the stress triaxiality, $\mu = (2\sigma_{II} - \sigma_I - \sigma_{III}) / (\sigma_I - \sigma_{III})$ is the Lode parameter, and $\sigma_I \ge \sigma_{II} \ge \sigma_{III}$ are the ordered principal stresses. Being a single parameter model, the Cockcroft-Latham criterion is easy to calibrate, and the fracture parameter is estimated as

$$W_C = \int_0^{p_f} \langle \sigma_I \rangle \, dp \tag{7}$$

where p_f is the equivalent strain at onset of fracture. However, in contrast to using a constant fracture strain, the Cockcroft-Latham criterion does take into account the effect of the hydrostatic and deviatoric stress state.

Since the component tests were to be modelled by larger shell elements, a simulation of the uniaxial tension test with 3 mm shell elements (LS-DYNA Type 1) was carried out to calibrate W_C. As can be seen from Fig. 1(b), the engineering stress-strain curve from the shell element simulation displays a stiffer post-necking behaviour than the solid element simulation. Ehlers and Varsta [41] proposed a solution to this discretization size effect by reducing the post-necking hardening for increasing element size. In the present study, the estimated post-necking hardening is considered a material property, and the same true stress-plastic strain curve is used as input in the shell element simulation of the tensile test.

The fracture parameter was determined from Eq. (7) by considering the element with most severe deformation. Since the simulated engineering stress-strain curve overestimates the post-necking stress level, a conservative value of W_C is found by assuming fracture to take place when the engineering strain in the simulation reaches the same value as the engineering strain at fracture in the experiment. This approach gives $W_C = 407\ \text{MPa}$, as shown in Fig. 1(b). A non-conservative estimate, $W_C = 621\ \text{MPa}$, is found by assuming fracture to occur when the simulated stress value reaches the final stress value in the experiment, see Fig. 1(b). In the present study, the average of the these two values was adopted, i.e., W_C was set to 514 MPa.

To check whether or not the deviations in the engineering stress-strain curve obtained with shell elements has some bearing on the estimated value of W_C, an alternative approach was employed. A simulation of the uniaxial tension test with the solid element model was conducted, where a 0.0001 mm thick membrane element with 3 mm in-plane size was added to the surface in the most deformed region inside the local neck, see Fig. 9(a). The point of fracture in the solid element simulation is readily found because the simulated engineering stress-strain curve is close to the experimental ones, see Fig. 1(a). The stress and strain histories of the membrane element were used to estimate the fracture parameter and the result was $W_C = 584\ \text{MPa}$, which is in the same range as the average value obtained in the shell element analysis. For comparison, the most deformed solid element had $W_C = 1025\ \text{MPa}$ at the same time instant, which clearly shows the large influence of discretization when it comes to prediction of ductile fracture in tests with high gradients in the stress and strain fields.

By assuming proportional loading and neglecting rate effects, combination of Eqns. (4), (6) and (7) gives the fracture strain according to the Cockcroft-Latham criterion as function of stress state, viz.

$$p_f(\sigma^*, \mu) = \left(\frac{n+1}{K} \left(\frac{W_C\sqrt{3+\mu^2}}{\left\langle \sigma^*\sqrt{3+\mu^2} + 1 - \mu/3 \right\rangle} - \sigma_0 p_L \right) + \left(p_L + p_0\right)^{n+1} \right)^{\frac{1}{1+n}} - p_0 \qquad (8)$$

Fig. 10(a) shows the fracture surface obtained from Eq. (8) in the range $-1/3 \le \sigma^* \le 2/3$ for the calibrated Domex 355 MC E material. As can be seen from Fig. 10 (a), the Cockcroft-Latham criterion predicts a decrease in ductility for increasing triaxiality at a constant value of the Lode parameter, and an increase in ductility with increasing Lode parameter for a constant value of triaxiality. Under plane stress conditions, the stress triaxiality is bounded to the region $-2/3 \le \sigma^* \le 2/3$ and, furthermore, the Lode parameter can be expressed as a function of the stress triaxiality. Thus, the fracture strain can be expressed in terms of stress triaxiality alone, and the resulting fracture locus for plane stress conditions is shown in Fig. 10 (a) and (b). Note that the Cockcroft-Latham criterion predicts no fracture for $\sigma^* \le -1/3$ in plane stress states, while for general 3D stress states it predicts fracture for values of σ^* down to $-2/3$ in the case of $\mu = -1$.

4.2 Finite element modelling

Finite element simulations of the steel panels were run with the explicit solver of LS-DYNA [49]. In the simulations with quasi-static loading, uniform mass scaling by a factor 10^7 was applied to reduce the computational time. To ensure appropriate boundary conditions, the whole test rig frame was included in the finite element models of the steel panel tests. The different parts of the model with the hemispherical indenter are presented in Fig. 11(a). To properly capture the buckling between the centre stringers, a clearance of half the plate thickness was introduced between the specimen and the top and bottom frames, and a geometrical imperfection following a sine wave with amplitude 0.5 mm and wavelength 50 mm was added to the plate between the centre stringers. The geometrical imperfection is indicated in Fig. 11(b). The clearance between the specimen and the test rig frame was necessary to achieve buckling deformations with the same magnitude as in the experiments, while the geometrical imperfection accounts for both the geometrical and material imperfections in the specimen.

The steel panel was discretized by quadrilateral Belytschko-Tsay shell elements (LS-DYNA type 2) with an initial element size of 25 mm. In the refined mesh along the boundary of the plate, two subdivisions were carried out resulting in elements with an initial size of 6.25 mm, see Fig. 11(b). Mesh refinement was also carried out in the region that was in contact with the indenter; here three subdivisions resulted in an initial element size of 3.125 mm, see Fig. 11(b). Contact between the specimen and the test-rig frame was handled by the automatic surface-to-surface contact description, using the shell element thickness as the contact thickness. The contact between the specimen and the indenter was handled by the surface-to-surface contact description. In this case, the contact constraint was imposed in the centre of the shell. In the contact between the indenter and the specimen, a Coulomb friction model was assigned with static and sliding friction coefficients equal to 0.3. In the specimen-top frame and the specimen-shim plate interfaces, zero friction was assumed, since a Teflon layer was positioned here in the experiments. The Teflon sheets were not included as separate parts in the numerical model.

All the parts in the finite element model had the same elastic behaviour as the steel panels. The test rig frame and the bolts were described by a linear elastic material model, while the shim plates, which experienced some plastic deformation, followed J_2 flow theory with elastic-perfectly plastic behaviour and a yield stress of 355 MPa. The stiffened panels were modelled by the rate-dependent J_2 flow theory, as described in Section 4.1. The indenters were modelled as rigid bodies. In the low-velocity simulations, the density of the indenter was adjusted so that the total impacting mass corresponded to the impacting mass in the experiments. All parts were discretized with quadrilateral Belytschko-Tsai shell elements, except the bolts which were discretized with beam elements having a cylindrical cross section. The shell elements were integrated in the thickness direction following a 7-point Gauss quadrature. The initial element size used for the test rig frame, shim plates and indenter were 15 mm, 7.5 mm and ~2.5 mm, respectively. Fracture of the steel panels was modelled by means of the element deletion method. When Cockcroft-Latham integral W reached the critical value W_C in one integration point, the components of the stress tensor were set to zero in all integration points within the element.

4.3 Numerical results

Fig. 12 compares the force-displacement curves from simulations with the experimental data. The predictions are found to be more accurate for the low-velocity impact tests than for the quasi-static tests. Both the force-displacement curves and failure are well predicted for the dynamic tests. In the simulations of the quasi-static tests with the cylindrical indenter, the force level is accurate up to a displacement of about 40 mm, then the force is somewhat overestimated up to a displacement of about 80 mm, and in the final part of the test the force is underestimated. The latter discrepancy might be due to onset of damage in the Teflon sheets in the tests, which increased the friction between the steel panel and the test rig frame. In the simulation of the quasi-static test with hemispherical indenter, the force is accurately estimated up to a displacement of about 70 mm, after which the force is overestimated until failure occurs somewhat prematurely. It is believed that the overestimation of the force level in these simulations is related to the modelling of the rather complex boundary conditions of the stiffened plates. Notably the simulations with quasi-static and dynamic loading produce similar force-displacement curves.

Two quasi-static simulations with the cylindrical indenter were run. In each simulation, the indenter was reversed at a displacement corresponding to the maximum displacement in one of the duplicate tests, see Fig. 12(a). Even if the force level is overestimated in the simulations, the elastic unloading stiffness is very similar to the experimental one. Also, the unloading stiffness in the low velocity simulations is in close agreement with the experimental unloading stiffness. As in the experiments, the low-velocity simulation with hemispherical punch and $v_0 = 4.49$ m/s rebounded from the steel panel, while the $v_0 = 5.7$ m/s simulation penetrated the target, see Fig. 12(d). The quasi-static and low-velocity simulations with hemispherical indenter display failure at approximately the same displacement. Thus, the difference in displacement at failure observed in the experiments is not reproduced in the simulations. The apparent strain-rate effect on the material's ductility could be accounted for in Eq. (7) by making the fracture parameter an explicit function of the strain rate, viz. $W_C = W_C(\dot{p})$. However, this would require more tests for calibration.

Fig. 13(a) and (b) shows the global deformation pattern in the quasi-static simulations with the cylindrical and hemispherical indenters, respectively. The low-velocity simulations had similar deformation patterns. Clearly a larger part of the specimen is activated in plastic deformation when the load is provided by the cylindrical indenter. As in the experiments, the centre stringers experienced an inward lateral deformation mode when loaded by the cylindrical indenter, while loading from the hemispherical indenter resulted in an outward deformation mode. The simulations with both indenters resulted in a sinusoidal deformation pattern between the stringers at the boundaries, as observed in the experiments, see Fig. 13(c) and (d). Necking and crack formation in the low-velocity simulation with the hemispherical punch are displayed in Fig. 14. In contrast to the experiments, the simulations did not display a loading-rate dependent fracture pattern; for both loading rates, a similar pattern with three radial cracks appeared. The deformation plots in Fig. 14(a)–(d) correspond to the points (a)–

(d) in the force-displacement curve denoted ‘Reference sim.’ in Fig. 15. As seen from Fig. 14, the largest strain concentration is centred near the apex of the indenter for small displacements and gradually moves in the radial direction for increased loading. Eventually local necking takes place approximately 27 mm in the radial direction from the centre of the indenter, leading to fracture.

4.4 Effect of spatial discretization

In order to illustrate the effect of spatial discretization on the steel-panel impact problem, additional simulations were carried out for the load case with the hemispherical indenter and initial indenter velocity of 5.7 m/s. In the three additional simulations, the initial characteristic element size in the region loaded by the indenter was 25 mm, 12.5 mm and 6.25 mm. The force-displacement curves are presented in Fig. 15 and compared with those from the experiments and the simulation with the reference mesh. As can be seen, the global force-displacement response is nearly independent of element size. On the contrary, onset of fracture, as indicated by a rapid drop in force level, is highly element-size dependent; the simulation with 6.25 mm elements overestimates the indenter displacement at fracture by ~20 mm, while the simulations with larger elements do not predict fracture at all. Onset of fracture is governed by Eq. (7) which relies on local stress and strain values. Prior to fracture, local necking takes place, and this phenomenon is not properly captured by the models with larger elements. Thus, the large-element models give non-conservative results for the displacement at fracture. It is noted that the fracture parameter, W_C, was calibrated from a simulation of the tensile test with element size ~3 mm. It is reasonable to assume that a calibration based on simulations with elements of about equal size to those used in the impact simulations would have given more accurate predictions.

4.5 Damage driven h-adaptivity

As indicated in the previous section, it can be beneficial to reduce the element size in the impact region if the aim is to accurately describe failure and crack propagation. In a simulation of a large scale structure, mesh refinement can be carried out by the analyst before starting a simulation, but in case the refinement is conducted on a too small region, a rerun of the simulation with a new mesh has to be performed. The analyst also risks refining an overly large region, which results in longer computational time than necessary. To overcome this problem, damage driven h-adaptivity was applied in simulations of the stiffened steel plates. The h-adaptivity is based on the fission adaptivity proposed by Belytschko et al. [50].

In the damage driven h-adaptivity, an element is subdivided into sibling elements with a characteristic element size of $h/2$ as W reach the value $W_1 = \int_0^{p_1} \langle \sigma_I \rangle dp$ in an integration point. Here h refers to the characteristic element size before subdivision. This subdivision may be repeated for new critical values, $W_m = \int_0^{p_m} \langle \sigma_I \rangle dp$, giving elements with a size of $h/2^m$. The additional node on the subdivided element adjoining a side of a larger neighbour element is constrained by interpolation of the displacement fields of the neighbour element, see [49] for more details. It was found that deleting a subdivided element adjoining a larger element resulted in numerical instabilities. To avoid this, all the neighbouring elements within a prescribed radius were subdivided when W_m was reached in a given element. A version of LS-DYNA was tailored-made for running these simulations.

In the following, a simulation of the low-velocity test with the hemispherical indenter and $v_0 = 5.7$ m/s is presented, where a maximum of three subdivisions was allowed. The initial element size was 25 mm, while the final element size after 3 subdivisions was $h/2^3 = 3.125$ mm. The radius defining the neighbourhood for subdivision was set to $2h$ = 50 mm to ensure that a sufficient number of elements were subdivided in order to avoid numerical instabilities. The subdivisions were conducted for W equal to $W_1 = 0.075W_C$, $W_2 = 0.37W_C$ and $W_3 = 0.63W_C$. These values of W correspond in turn to equivalent plastic strains of $p_1 = n/2 - p_0$, $p_2 = 2n - p_0$ and $p_3 = 3n - p_0$ in uniaxial tension when ignoring rate sensitivity.

The h-adaptivity simulation provides a similar response of the steel panel as the fixed mesh simulation with 3.125 mm large elements in the fracture region. Fig. 15 shows the force-displacement curves, while the local fracture pattern is shown in Fig. 16. The radius of the local neck at fracture is ~27 mm in the h-adaptivity simulation as in the fixed mesh simulation. In the present implementation of the h-adaptivity, the computational cost is 4-5 times lower than in a simulation where the whole steel panel is discretized by 3.125 mm elements, but still 3-4 times higher than in a simulation with refined mesh in the loading area, as shown in Fig. 11(b). However, when modelling a complex structure, extra computational costs due to h-adaptivity may be spared in the total time consumption for the analyst, since there is no need for defining regions with finer mesh before starting the simulation with the risks mentioned above.

5 Conclusions

An experimental study was conducted on stiffened steel panels subjected to transverse quasi-static and low-velocity loading by an indenter. The quasi-static and low-velocity tests display similar behaviour in terms of global force-displacement response, although the displacement at fracture is larger in the quasi-static tests. Nonetheless, the quasi-static tests are deemed to provide a good reference for low-velocity impact loading situations. The finite element simulations predicted the force-displacement response and failure with good accuracy for the low-velocity impact tests. On the contrary, errors occurred in the simulations of the quasi-static tests, which at least partly were ascribed to the complex boundary conditions. Fine spatial discretization was needed in the simulations to capture the onset of fracture. Automatic mesh refinement based on damage driven h-adaptivity was shown to predict local deformations and fracture of the steel panels with the same accuracy as a comparable simulation with a fixed mesh, but at a lower computational cost.

Acknowledgement

The financial support of this work from Centre for Advanced Structural Analysis (CASA), Centre for Research-based Innovation (CRI) at the Norwegian University of Science and Technology (NTNU), is gratefully acknowledged.

References

[1] Paik, J. K. and Thayamballi, A. K. (2003). Ultimate Limit State Design of Steel-Plated Structures. Chichester, West Sussex PO19 8SQ, England, John Wiley & Sons.
[2] Backman, M. E. and Goldsmith, W. (1978). The mechanics of penetration of projectiles into targets. International Journal of Engineering Science **16**(1): 1-99.
[3] Simonsen, B. C. and Lauridsen, L. P. (2000). Energy absorption and ductile failure in metal sheets under lateral indentation by a sphere. International Journal of Impact Engineering **24**(10): 1017-1039.
[4] Oberkampf, W. L. and Roy, C. J. (2010). Verification and Validation in Scientific Computing, Cambridge University Press.
[5] Langseth, M. and Larsen, P. K. (1994). Dropped objects' plugging capacity of aluminium alloy plates. International Journal of Impact Engineering **15**(3): 225-241.
[6] Wen, H. M. and Jones, N. (1994). Experimental Investigation into the Dynamic Plastic Response and Perforation of a Clamped Circular Plate Struck Transversely by a Mass. Journal of Mechanical Engineering Science **208**(113): 113-137.
[7] Wen, H. M. and Jones, N. (1996). Low-Velocity Perforation of Punch-Impact-Loaded Metal Plates. Journal of Pressure Vessel Technology **118**: 181-187.
[8] Grytten, F., Børvik, T., Hopperstad, O. S. and Langseth, M. (2009). Low velocity perforation of AA5083-H116 aluminium plates. International Journal of Impact Engineering **36**(4): 597-610.
[9] Liu, B., Villavicencio, R. and Guedes Soares, C. (2013). Experimental and Numerical Plastic Response and Failure of Laterally Impacted Rectangular Plates. Journal of Offshore Mechanics and Arctic Engineering **135**(4): 041602-041602.
[10] Holmen, J. K., Hopperstad, O. S. and Børvik, T. (2015). Low-velocity impact on multi-layered dual-phase steel plates. International Journal of Impact Engineering **78**(0): 161-177.
[11] Langseth, M. and Larsen, P. K. (1990). Dropped objects' plugging capacity of steel plates: An experimental investigation. International Journal of Impact Engineering **9**(3): 289-316.
[12] Gruben, G., Langseth, M., Fagerholt, E. and Hopperstad, O. S. (2016). Low-velocity impact on high-strength steel sheets: An experimental and numerical study. International Journal of Impact Engineering **88**: 153-171.
[13] Nakajima, K., Kikuma, T. and Hasuka, K. (1968). Study on the formability of steel sheets. Report. 8517-8530.
[14] Langseth, M. and Larsen, P. K. (1993). Dropped objects' plugging capacity of stiffened panels. STRUCTURAL DYNAMICS, Eurodyn '93**:** 547-554.
[15] Alsos, H. S. and Amdahl, J. (2009). On the resistance to penetration of stiffened plates, Part I - Experiments. International Journal of Impact Engineering **36**(6): 799-807.
[16] Liu, B., Villavicencio, R. and Guedes Soares, C. (2015). Simplified analytical method to evaluate tanker side panels during minor collision incidents. International Journal of Impact Engineering **78**: 20-33.
[17] Cho, S.-R. and Lee, H.-S. (2009). Experimental and analytical investigations on the response of stiffened plates subjected to lateral collisions. Marine Structures **22**(1): 84-95.
[18] Gruben, G., Hopperstad, O. S. and Børvik, T. (2013). Simulation of ductile crack propagation in dual-phase steel. International Journal of Fracture **180**(1): 1-22.
[19] Johnson, G. R. and Cook, W. H. (1985). Fracture characteristics of three metals subjected to various strains, strain rates, temperatures and pressures. Engineering Fracture Mechanics **21**(1): 31-48.
[20] Samantaray, D., Mandal, S., Borah, U., Bhaduri, A. K. and Sivaprasad, P. V. (2009). A thermo-viscoplastic constitutive model to predict elevated-temperature flow behaviour in a

titanium-modified austenitic stainless steel. Materials Science and Engineering: A **526**(1–2): 1-6.
[21] Børvik, T., Hopperstad, O. S., Berstad, T. and Langseth, M. (2001). A computational model of viscoplasticity and ductile damage for impact and penetration. European Journal of Mechanics - A/Solids **20**(5): 685-712.
[22] Shima, S. and Oyane, M. (1976). Plasticity theory for porous metals. International Journal of Mechanical Sciences **18**(6): 285-291.
[23] Rousselier, G. (1987). Ductile fracture models and their potential in local approach of fracture. Nuclear Engineering and Design **105**(1): 97-111.
[24] Gurson, A. L. (1977). Continuum theory of ductile rupture by void nucleation and growth, 1. Yield criteria and flow rules for porous ductile media. Journal of Engineering Materials and Technology-Transactions of the ASME 99(1): 2-15.
[25] Cockcroft, M. G. and Latham, D. J. (1968). Ductility and the workability of metals. Journal of the Institute of Metals **96**: 33-39.
[26] Wilkins, M. L., Streit, R. D. and Reaugh, J. E. (1980). Cumulative-strain-damage model of ductile fracture: simulation and prediction of engineering fracture tests. Lawrence Livermore National Laboratory. Report.
[27] Bai, Y. and Wierzbicki, T. (2008). A new model of metal plasticity and fracture with pressure and Lode dependence. International Journal of Plasticity **24**(6): 1071-1096.
[28] Gruben, G., Hopperstad, O. S. and Børvik, T. (2012). Evaluation of uncoupled ductile fracture criteria for the dual-phase steel Docol 600DL. International Journal of Mechanical Sciences **62**: 133-146.
[29] Mohr, D. and Marcadet, S. J. (2015). Micromechanically-motivated phenomenological Hosford–Coulomb model for predicting ductile fracture initiation at low stress triaxialities. International Journal of Solids and Structures **67–68**: 40-55.
[30] Calle, M. A. G. and Alves, M. (2015). A review-analysis on material failure modeling in ship collision. Ocean Engineering **106**: 20-38.
[31] Wu, F., Spong, R. and Wang, G. (2004). Using Numerical Simulation to Analyze Ship Collision. ICCGS, Izu, Japan.
[32] Villavicencio, R. and Soares, C. G. (2011). Numerical plastic response and failure of a pre-notched transversely impacted beam. Ships and Offshore Structures **7**(4): 417-429.
[33] Liu, B., Villavicencio, R. and Guedes Soares, C. (2013). Shear and tensile failure of thin aluminium plates struck by cylindrical and spherical indenters. Ships and Offshore Structures **10**(1): 45-58.
[34] Marciniak, Z. and Kuczyński, K. (1967). Limit strains in the processes of stretch-forming sheet metal. International Journal of Mechanical Sciences **9**(9): 609-620.
[35] Stoughton, T. B. (2000). A general forming limit criterion for sheet metal forming. International Journal of Mechanical Sciences **42**(1): 1-27.
[36] Alsos, H. S., Hopperstad, O. S., Törnqvist, R. and Amdahl, J. (2008). Analytical and numerical analysis of sheet metal instability using a stress based criterion. International Journal of Solids and Structures **45**(7–8): 2042-2055.
[37] Alsos, H. S., Amdahl, J. and Hopperstad, O. S. (2009). On the resistance to penetration of stiffened plates, Part II: Numerical analysis. International Journal of Impact Engineering **36**(7): 875-887.
[38] Yamada, Y. (2006). Bulbous Buffer Bow: A Measure to Reduce Oil Spill in Tanker Collisions. Department of Mechanical Engineering. Lyngby, Denmark, Technical University of Denmark. **PhD**.
[39] Ehlers, S., Broekhuijsen, J., Alsos, H. S., Biehl, F. and Tabri, K. (2008). Simulating the collision response of ship side structures: A failure criteria benchmark study. International Shipbuilding Progress **55**(1-2): 127-144.

[40] Hogström, P. (2012). RoPax Ship Collision – a Methodology for Survivability Analysis Department of Shipping and Marine Technology. Gothenburg, Sweden, Chalmers University of Technology. **PhD**.
[41] Ehlers, S. and Varsta, P. (2009). Strain and stress relation for non-linear finite element simulations. Thin-Walled Structures **47**(11): 1203-1217.
[42] Storheim, M., Alsos, H. S., Hopperstad, O. S. and Amdahl, J. (2015). A damage-based failure model for coarsely meshed shell structures. International Journal of Impact Engineering **83**: 59-75.
[43] Fagerholt, E., Borvik, T. and Hopperstad, O. S. (2013). Measuring discontinuous displacement fields in cracked specimens using digital image correlation with mesh adaptation and crack-path optimization. Optics and Lasers in Engineering **51**(3): 299-310.
[44] Hanssen, A. G., Auestad, T., Tryland, T. and Langseth, M. (2003). The kicking machine: A device for impact testing of structural components. International Journal of Crashworthiness **8**(4): 385-392.
[45] Harris, C. and Stephens, M. (1988). A Combined Corner and Edge Detection. Proceedings of The Fourth Alvey Vision Conference**:** 147-151.
[46] Landkof, B. and Goldsmith, W. (1985). Petalling of thin, metallic plates during penetration by cylindro-conical projectiles. International Journal of Solids and Structures **21**(3): 245-266.
[47] Wierzbicki, T. (1999). Petalling of plates under explosive and impact loading. International Journal of Impact Engineering **22**(9–10): 935-954.
[48] Amini, M. R., Isaacs, J. B. and Nemat-Nasser, S. (2010). Experimental investigation of response of monolithic and bilayer plates to impulsive loads. International Journal of Impact Engineering **37**(1): 82-89.
[49] LSTC (1998). LS-DYNA THEORETICAL MANUAL, Livermore Software Technology Corporation.
[50] Belytschko, T., Wong, B. L. and Plaskacz, E. J. (1989). Fission-fusion adaptivity in finite elements for nonlinear dynamics of shells. Computers & Structures **33**(5): 1307-1323.

Tables and figures

Table 1 Chemical composition of Domex 355 MC E (in weight %).

C	Si	Mn	P	S	Cr	Ni
0.056	0.02	0.59	0.006	0.002	0.04	0.06
Mo	V	Cu	Al	Nb	N	C_{ekv}
0.02	0.01	0.01	0.037	0.023	0.006	0.17

Table 2 Overview of component tests

	Indenter	Test label	Fracture	Punch velocity
Quasi-static	C	QS-C1	No	10 mm/min
		QS-C2	No	
	H	QS-H1	Yes	
		QS-H2	Yes	
Low-velocity	C	LV-C1	No	4.95 m/s
	H	LV-H1	Yes	5.70 m/s
		LV-H2	Yes	5.72 m/s
		LV-H3	No	4.49 m/s

Table 3 Material parameters for Domex 355 MC E

σ_0	K	n	p_0	p_L	$\dot{p}_0$	c
404 MPa	772 MPa	0.0173	-0.00164	0.0240	0.001 s^{-1}	0.004

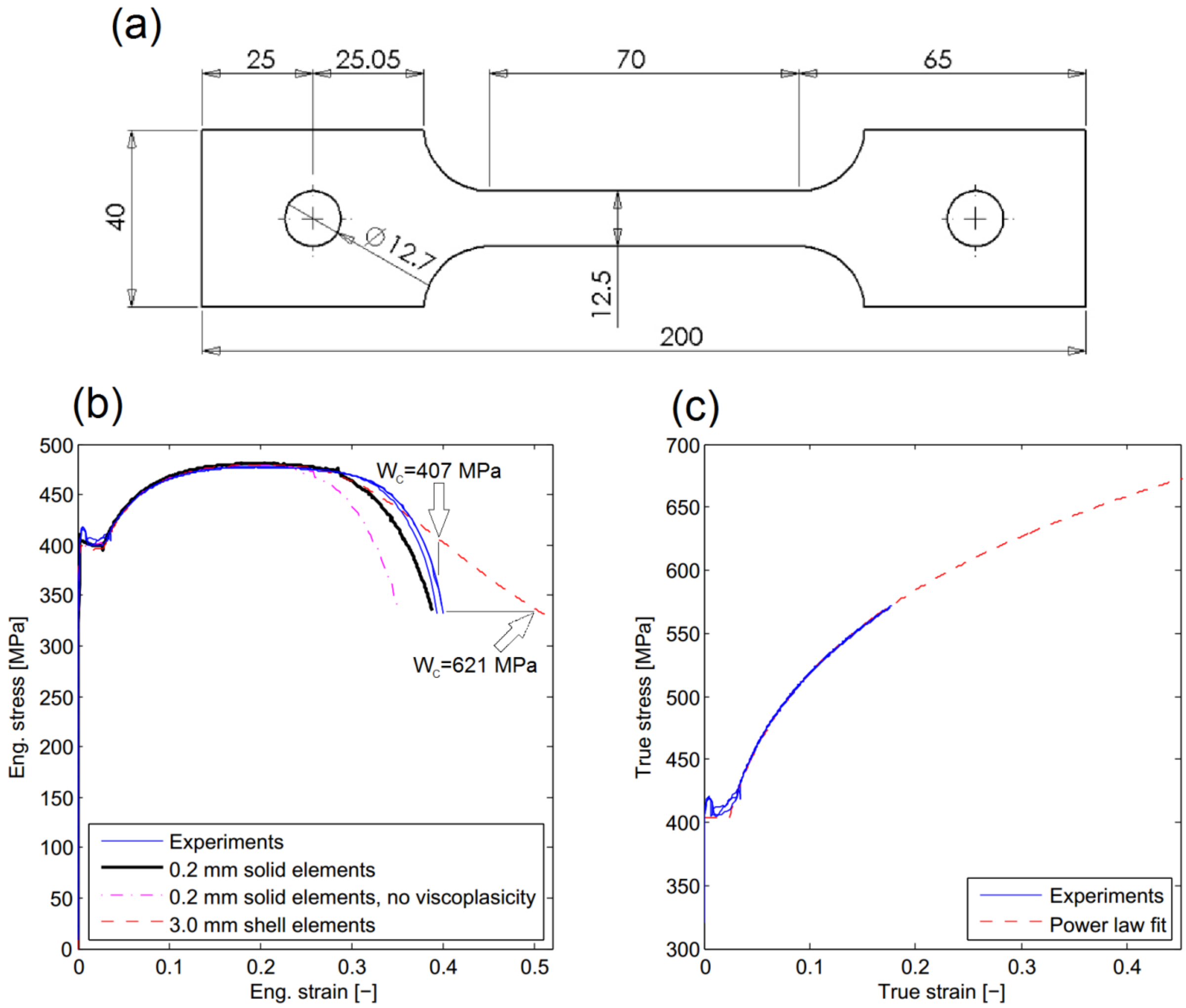

Fig. 1 (a) Nominal geometry of tensile specimen, (b) engineering stress-strain curves from experiments and finite element simulations, and (c) true stress-strain curves from tensile tests with power-law fit.

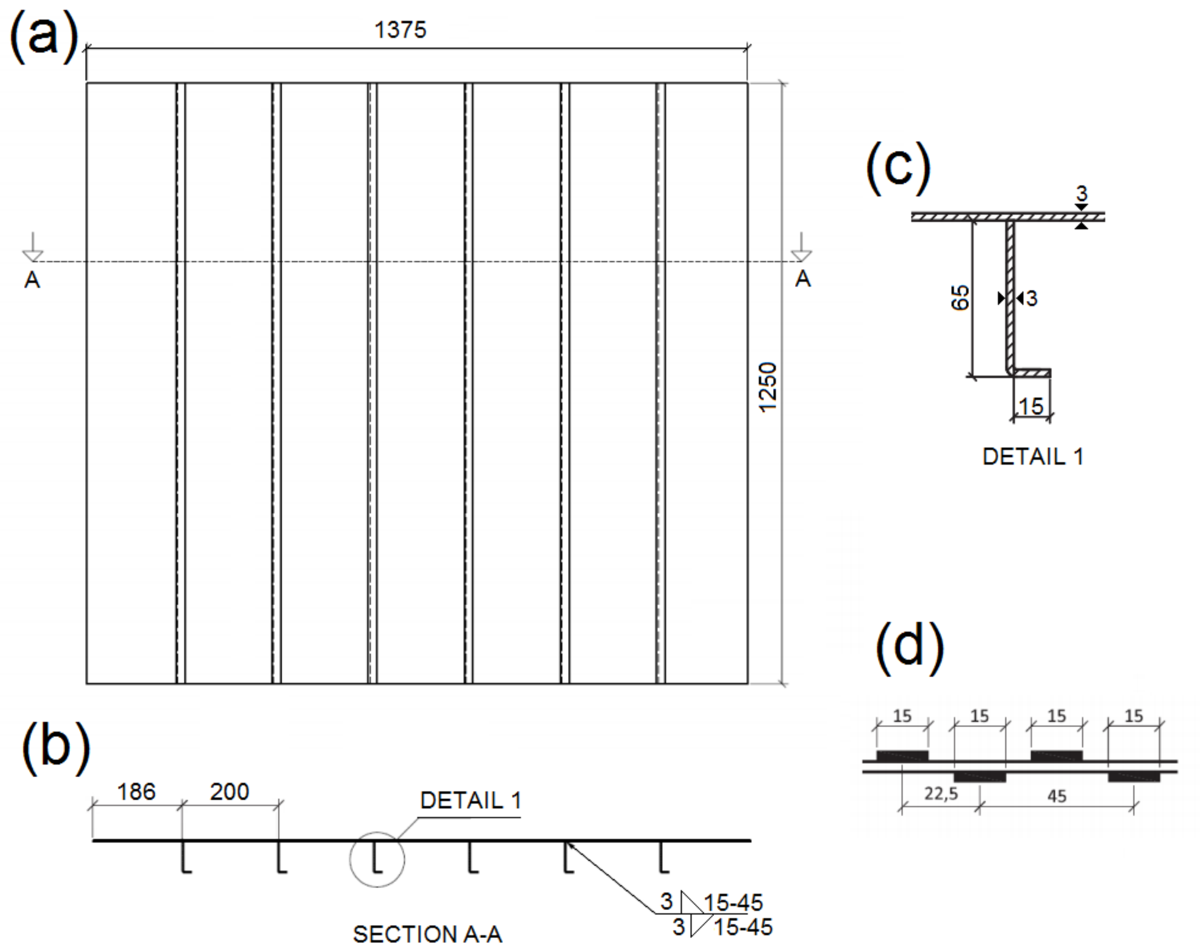

Fig. 2 (a) Stiffened steel plate seen from the side of the stiffeners, (b) cross section of test specimen, (c) detail of stiffener cross-section, and (d) length and centre-to-centre distance of the fillet welds.

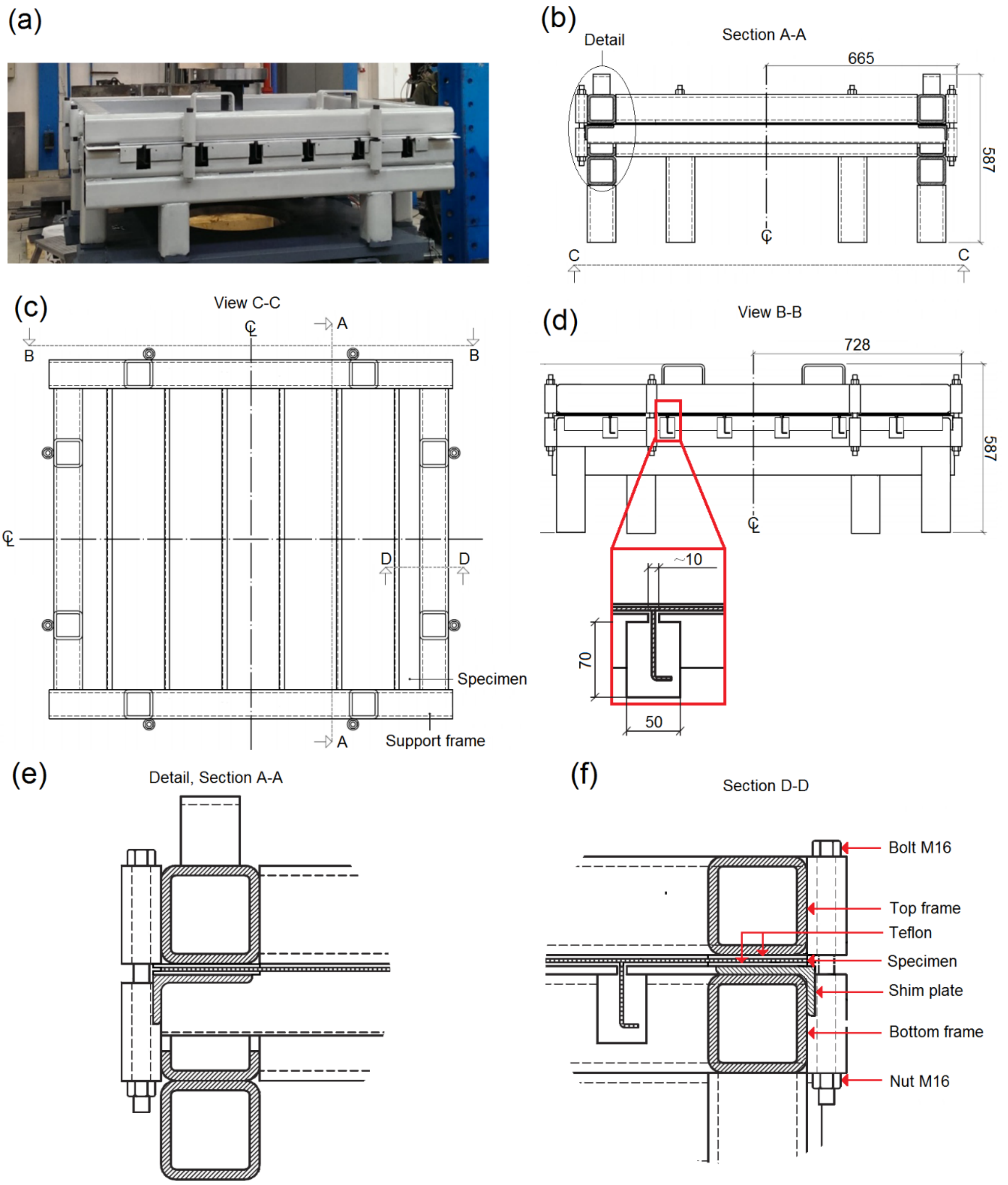

Fig. 3 (a) Specimen clamped between lower and upper support frame, (b) cross-section in the longitudinal direction, (c) schematic view from lower support frame side, (d) profile in the width direction, (e) details of cross section in longitudinal direction, and (f) details in cross section in width direction.

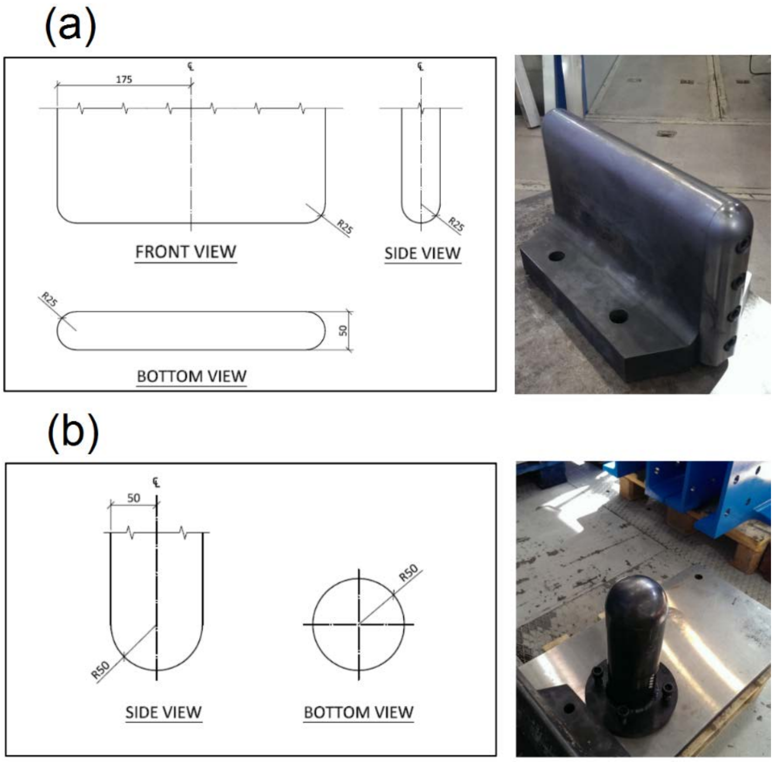

Fig. 4 Geometry of the two indenters: (a) rounded cylindrical indenter (type C), and (b) hemispherical indenter (type H).

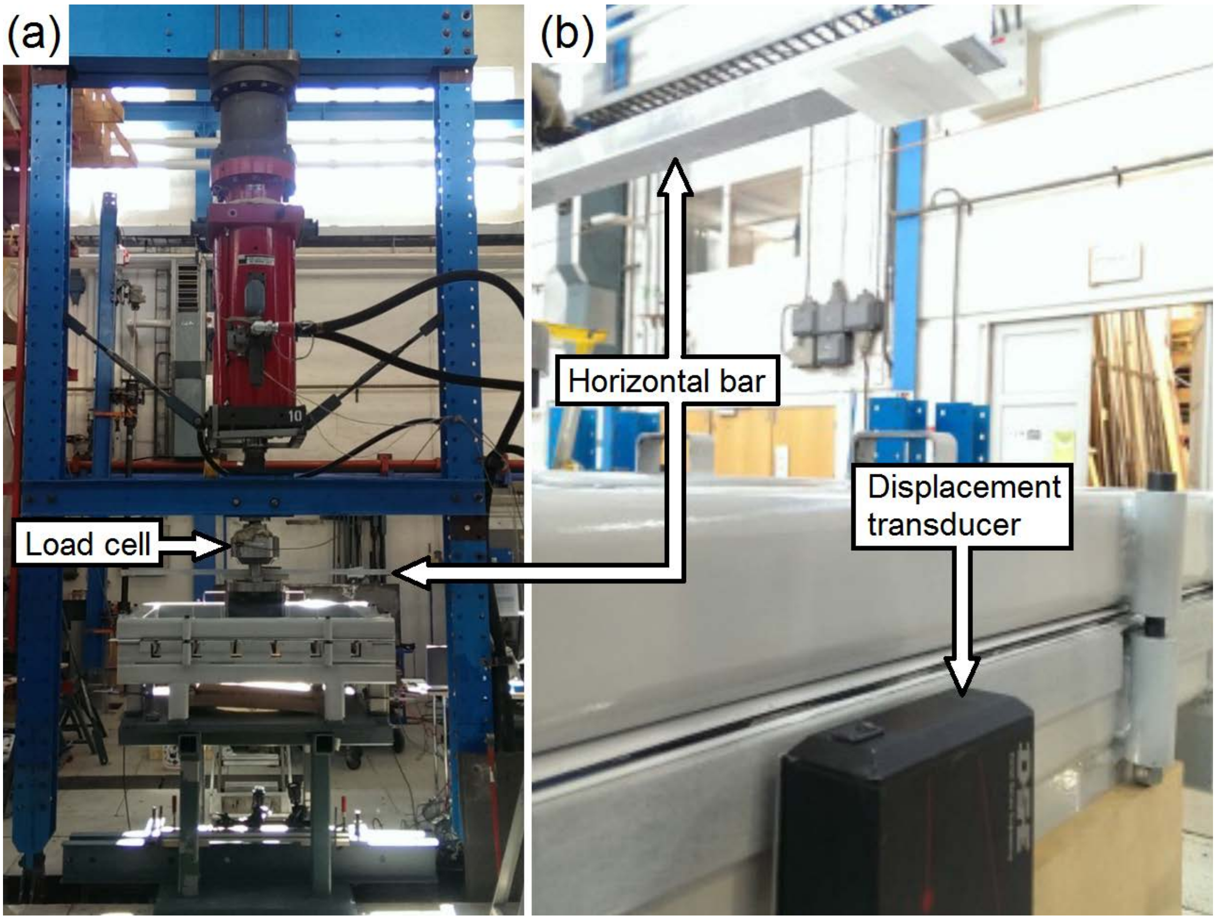

Fig. 5 (a) Test rig for quasi-static indentation tests, (b) position of one of the displacement transducers and the horizontal bar fastened to the load cell.

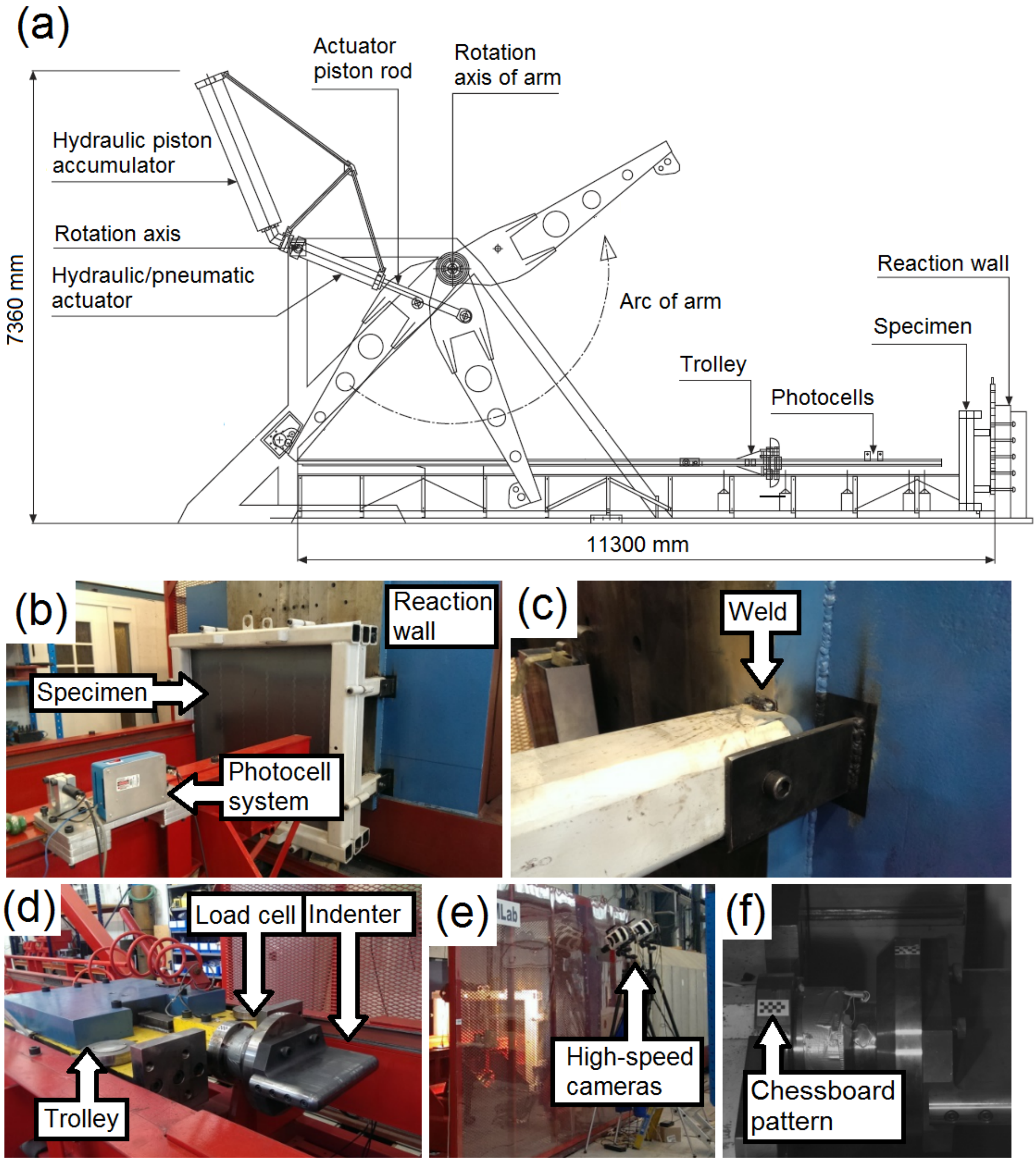

Fig. 6 (a) Schematic set-up of the pendulum impactor, (b) specimen and support frames fastened to the reaction wall, (c) detail from one leg of the lower support-plate fastened to reaction wall, (d) detail of load cell and indenter on trolley, (e) camera set-up for recording the impact tests and (f) load cell with chessboard pattern for optical displacement measurement.

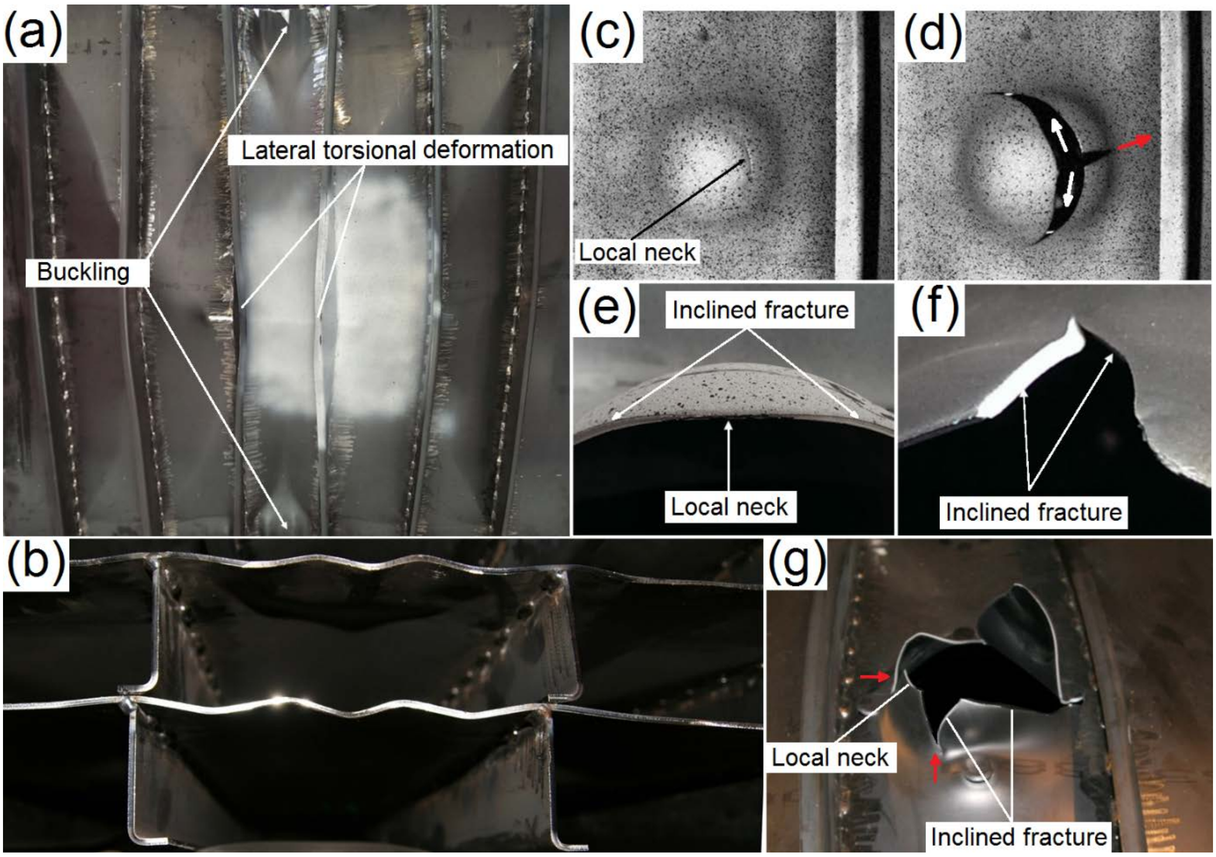

Fig. 7 (a) Post-test image of quasi-static test with the cylindrical indenter (QS-C1), (b) local buckling along plate boundary between the centre stringers, (c) image from quasi-static test with hemispherical indenter (QS-H1) before fracture and (d) image of the same test after fracture, (e) close up of region exposed to local necking and initial fracture, (f) close up of region exhibiting to radial crack path, (g) image of post-mortem low-velocity test with hemispherical indenter (LV-H1).

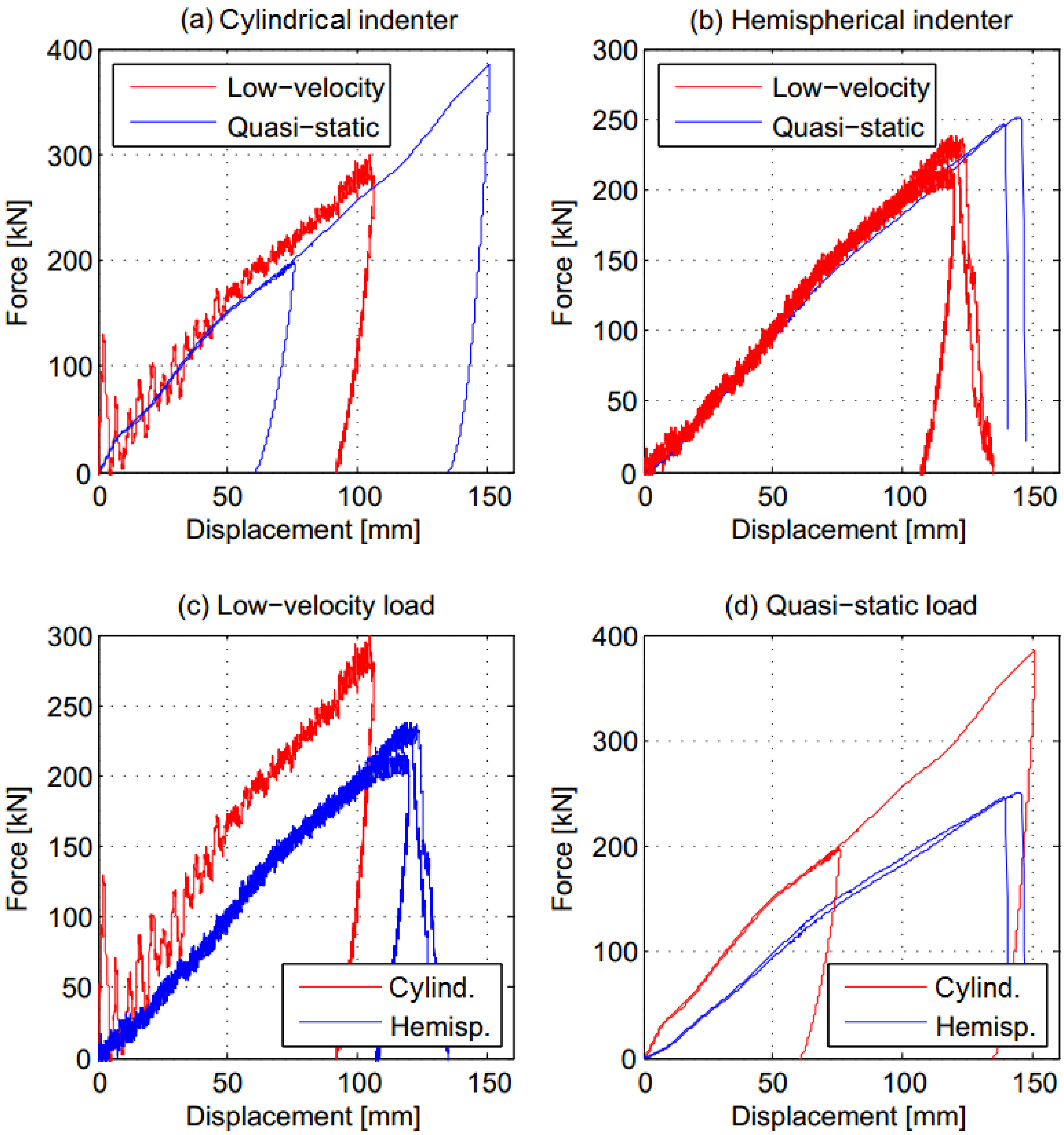

Fig. 8 Force-displacement curves from stiffened steel plate tests with (a) cylindrical and (b) hemispherical indenter and (c) low-velocity and (d) quasi-static loading.

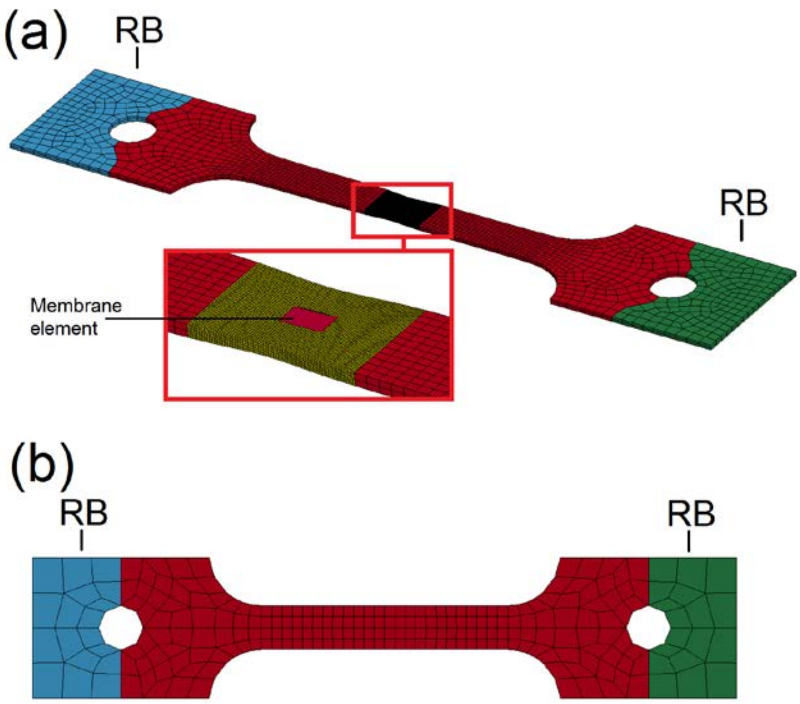

Fig. 9 Mesh of uniaxial tensile test: (a) solid elements and (b) shell elements. The prescribed velocities were applied on the rigid body (RB) parts.

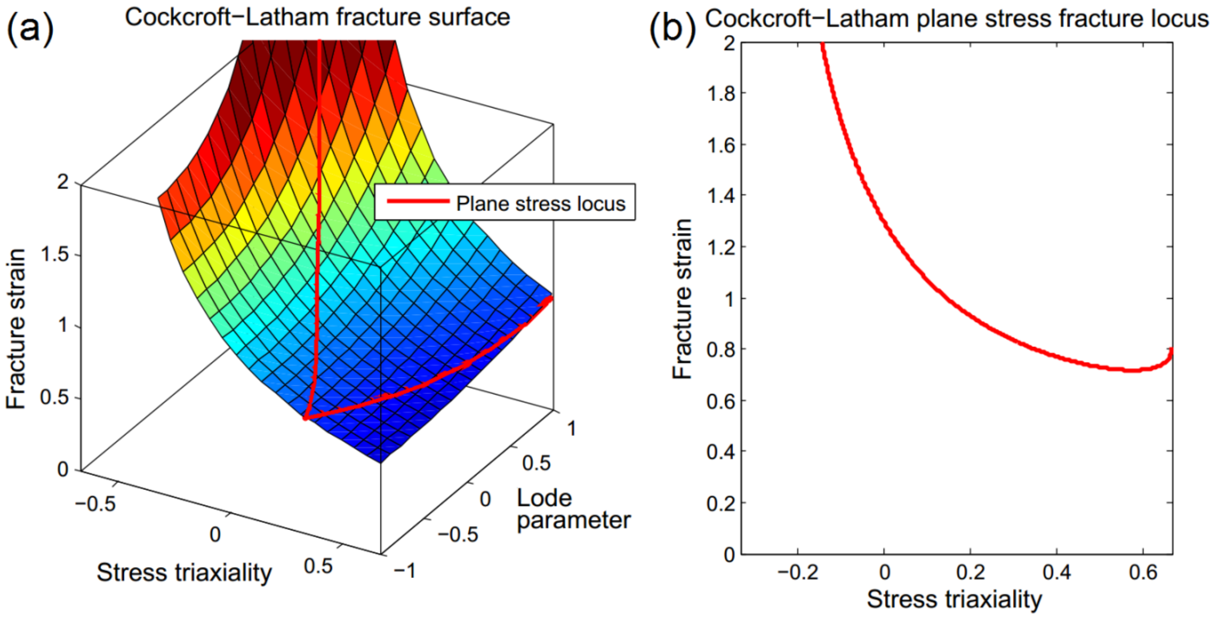

Fig. 10 (a) Fracture surface for 3D stress states and (b) fracture locus for plane stress states defined by the calibrated Cockcroft-Latham criterion. The plane-stress fracture locus is also shown in (a).

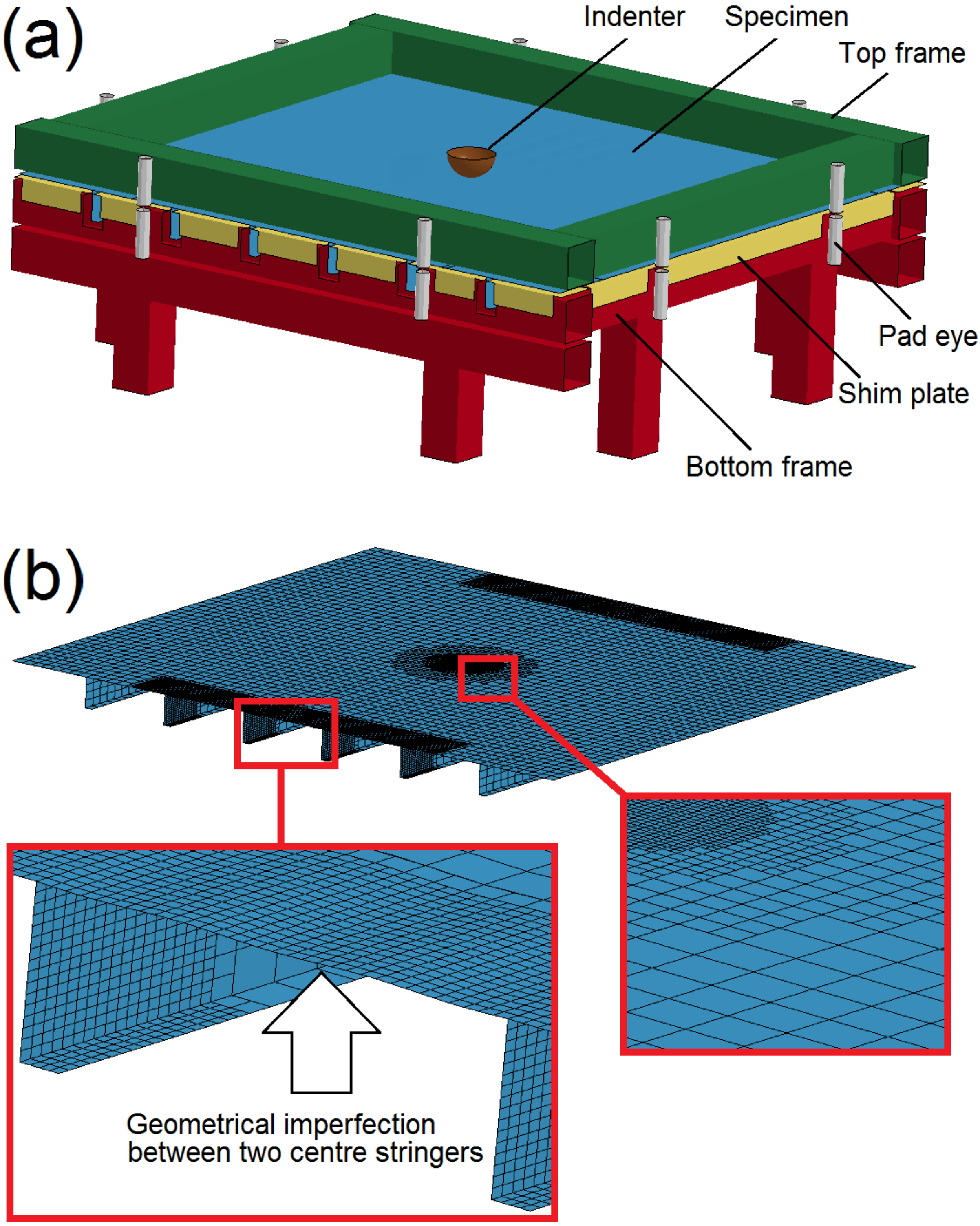

716

717 Fig. 11 (a) Parts in the finite element model and (b) discretization of specimen.

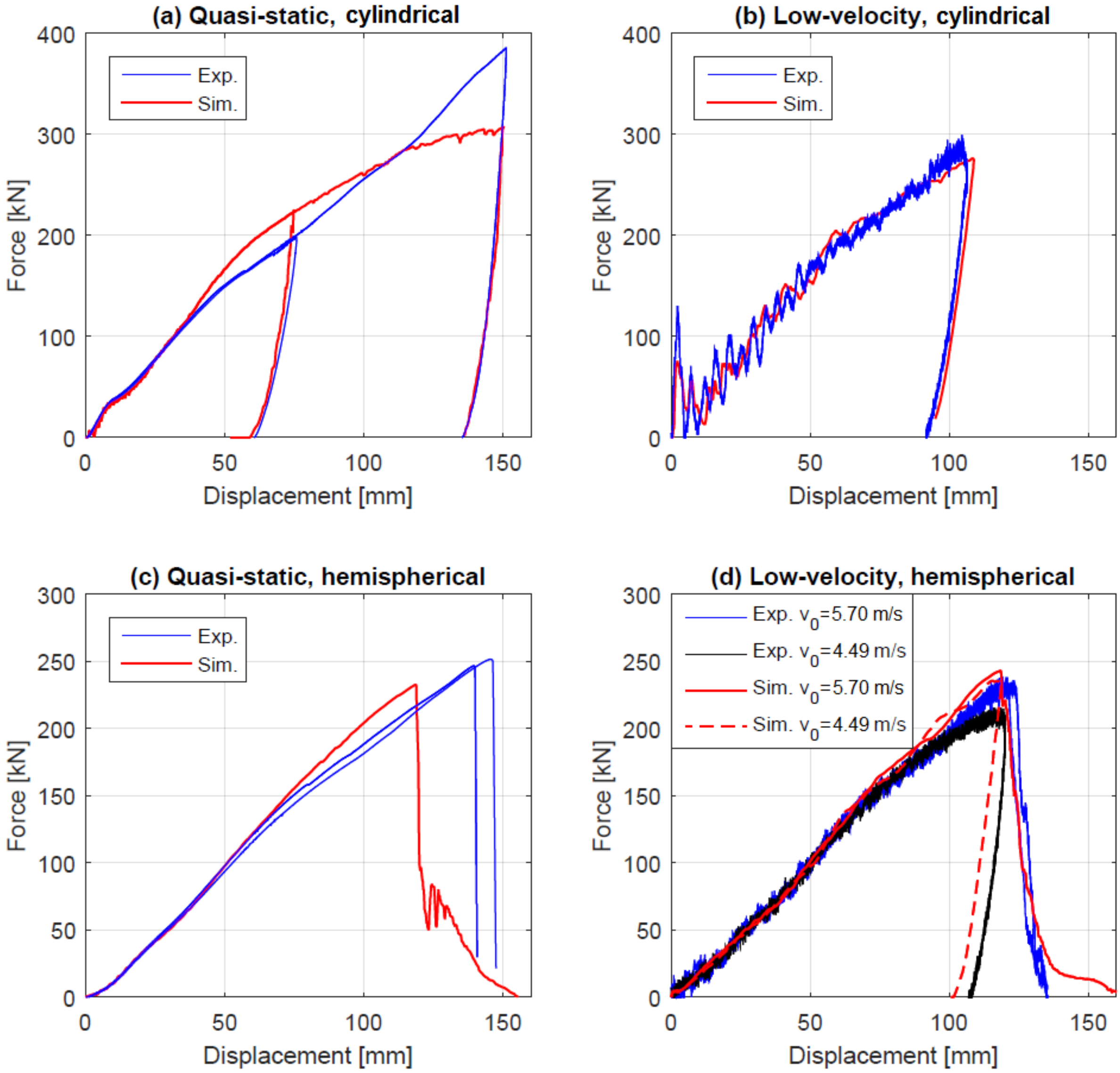

Fig. 12 Force-displacement curves from finite element simulations of the stiffened steel plate tests and comparison with experimental data: (a) quasi-static and (b) low-velocity loading with cylindrical indenter, and (c) quasi-static and (b) low-velocity loading with hemispherical indenter;

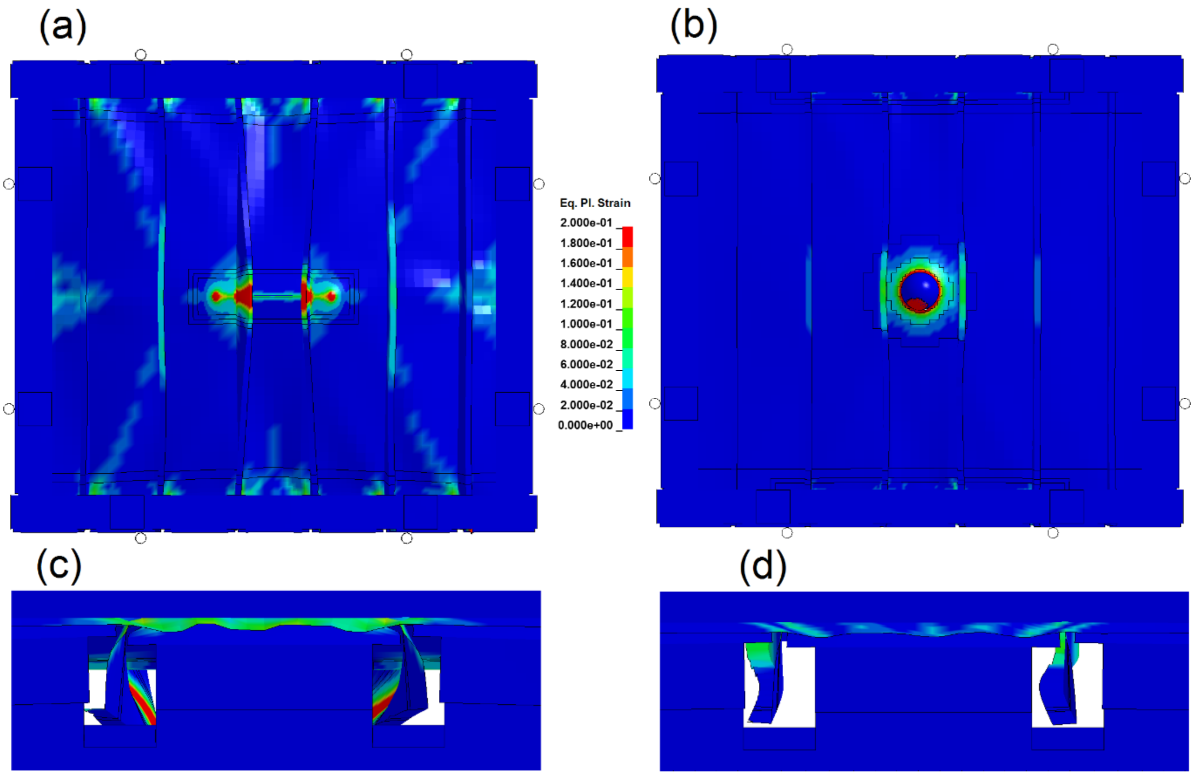

Fig. 13 Final deformation modes in quasi-static simulations with (a),(c) cylindrical indenter and (b),(d) hemispherical indenter. (The contour levels represent equivalent plastic strain.)

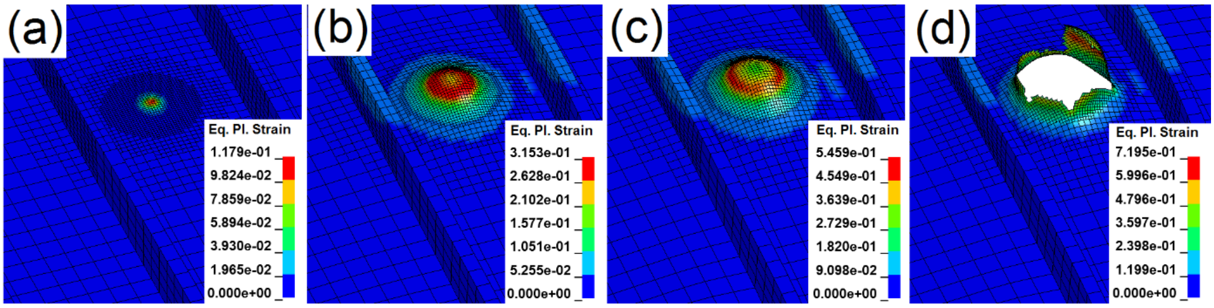

Fig. 14 Deformation and fracture in simulation with hemispherical indenter and impact velocity $v_0 = 5.7$ m/s. (The contour levels represent equivalent plastic strain.)

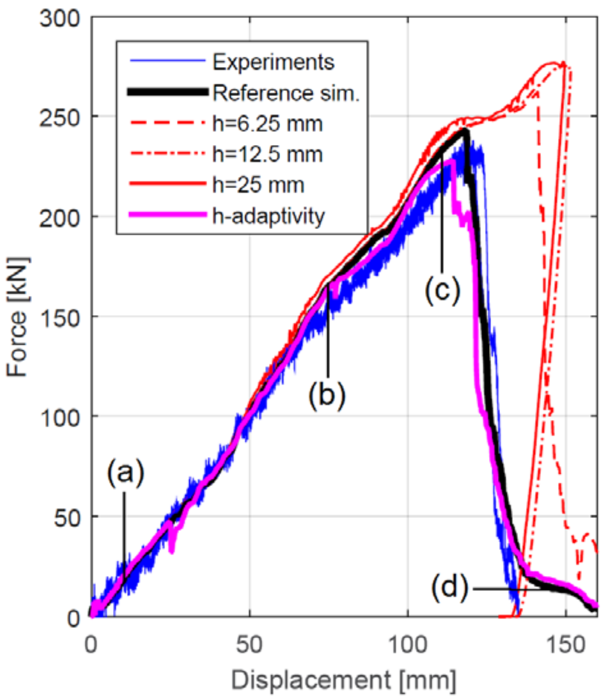

Fig. 15 Force-displacement curves from experiments and simulations with hemispherical indenter and impact velocity $v_0 = 5.7$ m/s. The points (a)–(d) refer to deformation plots in Fig. 14(a)–(d).

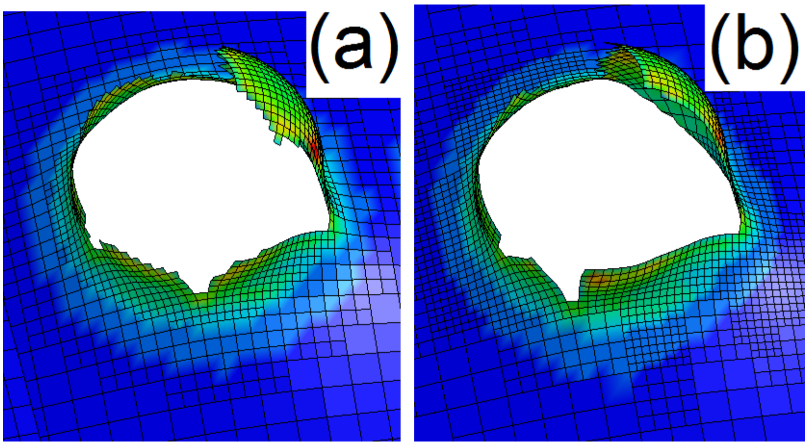

Fig. 16 Fracture pattern in simulations with hemispherical indenter and impact velocity $v_0 = 5.7$ m/s: (a) simulation with fixed mesh and (b) simulation with h-adaptivity.